

JWST COMPASS: The first near- to mid-infrared transmission spectrum of the hot super-Earth L 168-9 b

MUNAZZA K. ALAM,^{1,2} PETER GAO,² JEA ADAMS REDAI,³ NICOLE L. WALLACK,² NICHOLAS F. WOGAN,⁴ ARTYOM AGUICHINE,⁵ ANNE DATTILO,⁵ LILI ALDERSON,⁶ NATASHA E. BATALHA,⁷ NATALIE M. BATALHA,⁵ JAMES KIRK,⁸ MERCEDES LÓPEZ-MORALES,³ ANNABELLA MEECH,³ SARAH E. MORAN,⁹ JOHANNA TESKE,^{10,11} HANNAH R. WAKEFORD,⁶ AND ANGIE WOLFGANG¹²

¹*Space Telescope Science Institute, 3700 San Martin Drive, Baltimore, MD 21218, USA*

²*Carnegie Science Earth and Planets Laboratory, 5241 Broad Branch Road, NW, Washington, DC 20015, USA*

³*Center for Astrophysics | Harvard & Smithsonian, 60 Garden St, Cambridge, MA 02138, USA*

⁴*Space Science Division, NASA Ames Research Center, Moffett Field, CA 94035*

⁵*Department of Astronomy and Astrophysics, University of California, Santa Cruz, CA 95064, USA*

⁶*School of Physics, University of Bristol, HH Wills Physics Laboratory, Tyndall Avenue, Bristol BS8 1TL, UK*

⁷*NASA Ames Research Center, Moffett Field, CA 94035, USA*

⁸*Department of Physics, Imperial College London, Prince Consort Road, London, SW7 2AZ, UK*

⁹*Department of Planetary Sciences and Lunar and Planetary Laboratory, University of Arizona, Tucson, AZ, USA*

¹⁰*Earth and Planets Laboratory, Carnegie Institution for Science, 5241 Broad Branch Road, NW, Washington, DC 20015, USA*

¹¹*The Observatories of the Carnegie Institution for Science, 813 Santa Barbara St., Pasadena, CA 91101, USA*

¹²*Eureka Scientific Inc., 2452 Delmer Street Suite 100, Oakland, CA 94602-3017*

ABSTRACT

We present the first broadband near- to mid-infrared (3–12 μm) transmission spectrum of the highly-irradiated ($T_{\text{eq}} = 981\text{ K}$) M dwarf rocky planet L 168-9 b (TOI-134 b) observed with the NIRSpec and MIRI instruments aboard JWST. We measure the near-infrared transit depths to a combined median precision of 20 ppm across the three visits in 54 spectroscopic channels with uniform widths of 60 pixels ($\sim 0.2\ \mu\text{m}$ wide; $R \sim 100$), and the mid-infrared transit depths to 61 ppm median precision in 48 wavelength bins ($\sim 0.15\ \mu\text{m}$ wide; $R \sim 50$). We compare the transmission spectrum of L 168-9 b to a grid of 1D thermochemical equilibrium forward models, and rule out atmospheric metallicities of less than $100\times$ solar (mean molecular weights $< 4\ \text{g mol}^{-1}$) to 3σ confidence assuming high surface pressure (> 1 bar), cloudless atmospheres. Based on photoevaporation models for L 168-9 b with initial atmospheric mass fractions ranging from 2–100%, we find that this planet could not have retained a primordial H/He atmosphere beyond the first 200 Myr of its lifetime. Follow-up MIRI eclipse observations at $15\ \mu\text{m}$ could make it possible to confidently identify a CO_2 -dominated atmosphere on this planet if one exists.

Keywords: Exoplanet atmospheric composition (2021); Exoplanet atmospheres (487); Exoplanets (498); Infrared spectroscopy (2285)

1. INTRODUCTION

Atmospheric characterization of terrestrial, and potentially habitable, exoplanets is a key endeavor driving the focus of next-generation space-based facilities such as the Habitable Worlds Observatory (HWO; e.g., Checlair et al. 2021; Hall et al. 2023; Vaughan et al. 2023; Borges et al. 2024), the Large Interferometer for Exoplanets mission (LIFE; e.g., Defrère et al. 2018; Quanz 2021; Quanz et al. 2022; Matsuo et al. 2023), and ground-based extremely large telescopes (ELTs; e.g., Snellen et al. 2015; Hawker & Parry 2019; Leung et al.

2020; Currie et al. 2023; Zhang et al. 2024a). Although these future efforts are directed toward high-contrast imaging of terrestrial planets and detecting their atmospheres, progress toward these goals can already be made using transiting systems. Transiting terrestrial planets in nearby M dwarf systems in particular offer the most favorable prospects for spectroscopic observations due to their large planet-to-star radius ratios, frequent transit events, and close-in habitable zones (e.g., Dressing & Charbonneau 2015). However, intense X-ray and extreme-UV irradiation from M dwarf host stars

can result in significant atmospheric mass loss ($\sim 10^8$ – 10^{10} g s $^{-1}$; [Dos Santos et al. 2023](#)), thus influencing the persistence of substantial primordial (e.g., [Kasting & Pollack 1983](#); [Owen & Jackson 2012](#); [Rogers 2015](#); [Airapetian et al. 2017](#); [Rogers & Owen 2021](#)) or secondary ([Dong et al. 2018](#); [Kite & Barnett 2020](#)) atmospheres on rocky planets over their lifetimes.

Spectroscopic observations of small ($R \lesssim 1.7 R_{\oplus}$) planets orbiting nearby low-mass M dwarfs have not yet provided definitive evidence of the presence of a terrestrial planet atmosphere. Transmission spectroscopy of small planets with Hubble’s Widefield Camera 3 (WFC3; e.g., [de Wit et al. 2016, 2018](#); [Wakeford et al. 2019](#); [Damiano et al. 2022](#)) and large ground-based telescopes (e.g. [Diamond-Lowe et al. 2018, 2020, 2023](#)) have ruled out thick hydrogen/helium-dominated atmospheres for these planets. Higher mean molecular weight secondary atmospheres are possible ([Moran et al. 2018](#)), but the precision and resolution of these observations cannot explore this scenario.

With JWST’s exquisite precision, we can now begin probing the presence of secondary atmospheres on rocky planets. However, JWST transmission observations thus far have been challenging, since the predicted amplitude of atmospheric spectral features ($\lesssim 20$ ppm) is comparable to the expected pre-launch (~ 10 – 20 ppm; [Greene et al. 2016](#); [Rustamkulov et al. 2022](#)) and measured (~ 5 ppm; [Lustig-Yaeger & Fu et al. 2023](#)) instrument noise floors. To date, observations of rocky planets with JWST NIRSpec/G395H have yielded featureless transmission spectra ruling out atmospheres dominated by H/He, methane, or water ([Lustig-Yaeger & Fu et al. 2023](#)). However, interpretations of these spectra have been muddled by the influence of stellar activity ([Moran & Stevenson et al. 2023](#)), visit-to-visit variability ([May & MacDonald et al. 2023](#)), offsets between the NRS1 and NRS2 detectors, ([Damiano et al. 2024](#); [Wallack et al. 2024](#)), differences in data reductions ([Kirk et al. 2024](#)), and lower than expected transit depth precisions ([Alderson et al. 2024](#)). These astrophysical and instrumental systematics are clouding our holistic understanding of the atmospheric properties of small planets.

To better understand the prevalence and properties of small exoplanet atmospheres at the population level, the JWST COMPASS (Compositions of Mini-Planet Atmospheres for Statistical Study) program (GO 2512; PIs: [Batalha & Teske](#)) is obtaining NIRSpec/G395H transmission spectra for a sample of 11 quantitatively-selected 1–3 R_{\oplus} planets – including six targets with radii smaller than 1.7 R_{\oplus} . The program’s full statistical sample will include the addition of a target from GTO 1224. COMPASS aims to build a link between planetary de-

Table 1. System parameters for L 168-9 b.

Stellar Parameters	
K (mag)	7.082 ± 0.03^a
M_{\star} (R_{\odot})	0.62 ± 0.03^a
R_{\star} (R_{\odot})	0.600 ± 0.022^a
T_{eff} (K)	3800 ± 70^a
log(g) (cgs)	4.04 ± 0.49^a
[Fe/H] $_{\star}$	0.04 ± 0.17^a
Age (Gyr)	2.99 ± 0.64^b
Planetary Parameters	
Period (days)	1.40150 ± 0.00018^a
M_{P} (M_{\oplus})	4.60 ± 0.56^a
R_{P} (R_{\oplus})	1.39 ± 0.09^a
T_{eq} (K)	980 ± 20^a
Semi-major axis (AU)	0.02091 ± 0.00024^a

^a[Astudillo-Defru et al. \(2020\)](#) and references therein

^b[Engle & Guinan \(2023\)](#)

mographics and atmospheric characterization of super-Earths and sub-Neptunes by exploring the detectability of small planet atmospheres and their compositional diversity – thereby enabling population-level atmospheric constraints ([Batalha et al. 2023](#)). The focus of this study is one of the smallest and hottest COMPASS targets: L 168-9 b (TOI-134 b; [Astudillo-Defru et al. 2020](#)). L 168-9 b is a highly-irradiated ($T_{\text{eq}}=981$ K) planet, with a radius of 1.39 R_{\oplus} and a mass of 4.6 M_{\oplus} , in a 1.4 d orbital period around a bright ($K=7.1$) M1V star (see Table 1).

Here we present the 3–12 μm transmission spectrum of L 168-9 b using JWST NIRSpec/G395H observations obtained as part of the COMPASS program and MIRI/LRS data taken during commissioning (Program COM 1033; PI: [Kendrew](#)). The structure of this paper is as follows: We describe our observations in §2 and detail our data reduction techniques and light curve fitting methods in §3. In §4, we present the near- to mid-infrared transmission spectrum of L 168-9 b, and interpret our results using 1D thermochemical equilibrium forward models. We place L 168-9 b in the context of other rocky exoplanets, investigate its atmospheric loss history, and discuss future characterization opportunities in §5. We summarize our results in §6.

2. OBSERVATIONS

2.1. *NIRSpec*

We observed three transits of L168-9b with JWST NIRSpec (Near-InfraRed Spectrograph; Jakobsen et al. 2022; Birkmann et al. 2022) on UT 03 June 2023, 18 June 2023, and 27 June 2023 using the high-resolution (R \sim 2700) G395H mode, which provides spectroscopy between 2.87–5.14 μm across the NRS1 and NRS2 detectors (with a \sim 0.1 μm detector gap between 3.72–3.82 μm). The observations were taken with the NIRSpec Bright Object Time Series (BOTS) mode using the SUB2048 subarray, the F290LP filter, the S1600A1 slit, and the NRSRAPID readout pattern. Each 5.97 hr exposure consisted of 3359 integrations (divided into three segments) with four groups per integration, and was designed to be centered on the 1.3 hr transit event with sufficient out-of-transit baseline. The first visit suffered from a high gain antenna (HGA) move during UT 03 June 2023 around \sim MJD 60098.45027, affecting integrations \sim 1386-1392.

2.2. *MIRI*

A single transit of L168-9b was observed with JWST MIRI (Mid-InfraRed Instrument; Rieke et al. 2015a,b) on UT 29 May 2022 as part of commissioning activities to characterize the performance of the slitless Low Resolution Spectroscopy (LRS; Kendrew et al. 2015, 2018) mode for time-series observations (Bouwman et al. 2023). The observations were taken over a 4.14 hr exposure consisting of 9371 integrations with nine groups per integration and divided into five segments. The exposure was taken with the SLITLESSPRISM subarray, the F1000W filter, the FASTR1 readout pattern, and designed to cover sufficient pre- and post-transit baseline, detector settling time (\sim 30 minutes), and flexibility in scheduling. An HGA move occurred during the MIRI transit during integrations \sim 2878-2885 (\sim MJD 59728.39444).

3. DATA REDUCTION

We reduced our observations of L168-9b using three independent data reduction pipelines, which are described below: *Aesop* (§3.1.1), *Tiberius* (§3.1.2), and *Eureka!* (§3.1.3).

3.1. *NIRSpec G395H*

3.1.1. *Aesop*

Aesop is a JWST data reduction pipeline developed for the reduction and analysis of NIRSpec G395H observations that has been benchmarked with several other pipelines in the literature (see e.g., Alderson et al. 2023). In our analysis, we treated the data sets for the NRS1

and NRS2 detectors, as well as for each visit, separately. Starting with the raw uncalibrated JWST data products, we first ran the standard Stage 1 steps of the STScI *jwst* pipeline (version 1.8.2, context map 1078; Bushouse et al. 2022) for time-series observations, including corrections for saturation, bias, linearity, and dark current. We set the detection threshold for the jump step to 15, applied a custom group-level background subtraction to remove $1/f$ noise using a 15σ threshold and a second-order polynomial, and performed standard ramp fitting. We then used the standard steps for Stage 2 of the *jwst* pipeline to extract the integration exposure times and the 2D wavelength map.

We performed additional cleaning steps to replace poor data quality pixels (flagged as saturated, hot, dead, do not use, low quantum efficiency, or no gain value) with the median of the neighboring pixels and removed residual $1/f$ noise by calculating and subtracting the median pixel value of each column. To extract the 1D time-series stellar spectra, we fit a Gaussian profile to each column of a given integration to find the center of the spectral trace and smoothed the trace centers with a median filter, and then we fit a fourth-order polynomial to the smoothed trace centers. We extracted the 1D stellar spectra by summing up the flux within a 10-pixel wide aperture, calculating the uncertainties in the stellar spectra assuming photon noise. We obtained the shifts in the x and y pixel positions throughout the observation by cross-correlating the 1D stellar spectra to the first spectrum in the time-series.

We generated the broadband (white) light curves by summing up the stellar flux in the time-series between 2.862704–3.714356 μm for NRS1 and 3.819918–5.082485 μm for NRS2. For the spectroscopic light curves, we generated 54 binned light curves with uniform widths of 60 pixels (\sim 0.2 μm wide) based on the G395H wavelength solution. For both our white and spectroscopic light curves, we iteratively removed data points that were greater than 3σ outliers in the residuals and also re-scaled our flux uncertainties following Pont et al. (2006). We fit the broadband and spectroscopic light curves for NRS1 and NRS2 using a least-squares minimizer. We fit each light curve with a two-component function consisting of a transit model generated using *batman* (Kreidberg 2015) multiplied by a systematics model of the form:

$$S(\lambda) = c_0 + (c_1 \times x) + (c_2 \times y) + (c_3 \times t) \quad (1)$$

where x and y are the x - and y - pixel positional shifts on the detector, t is time, and the coefficients c_0 , c_1 , and c_2 are constants to be fit.

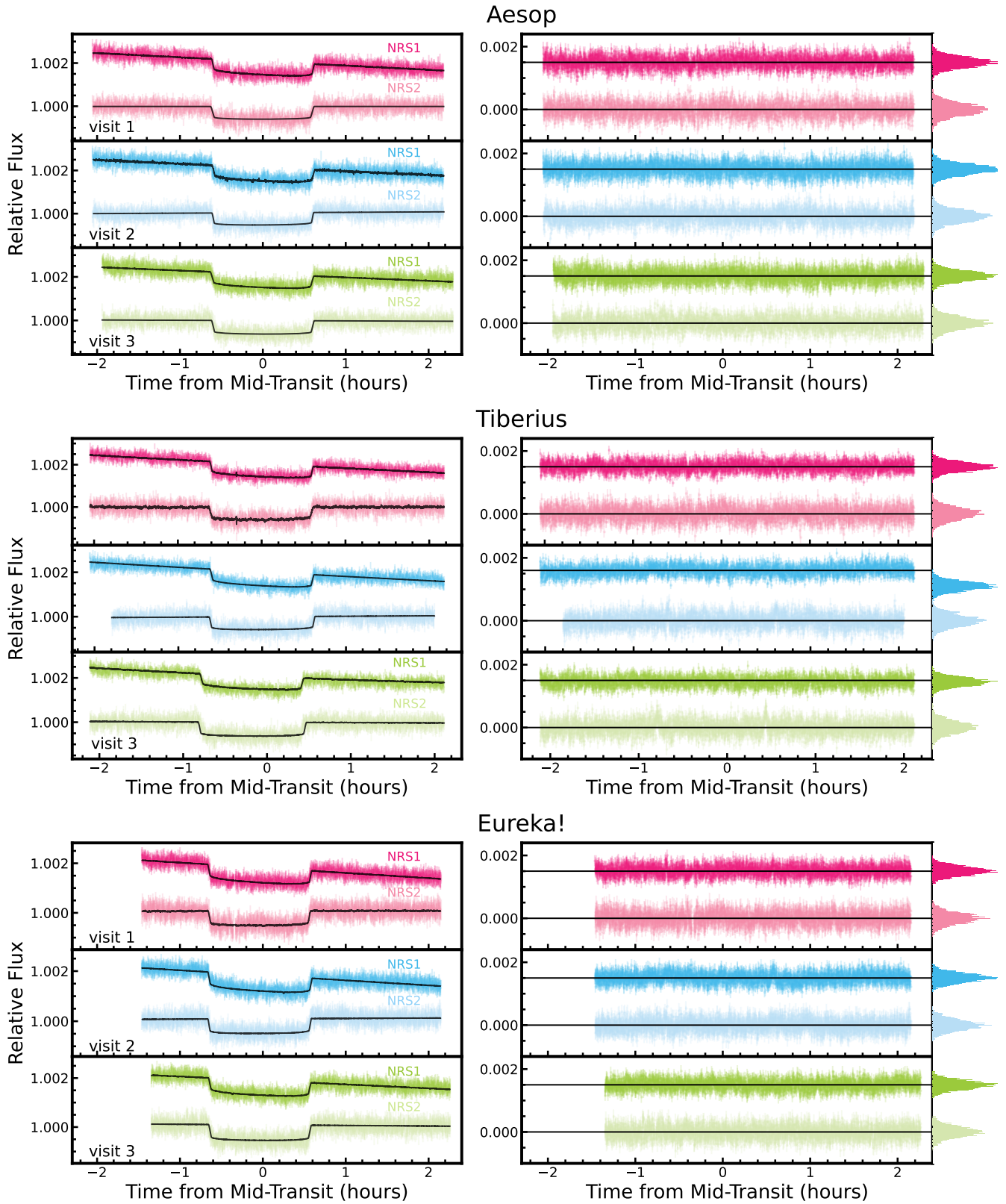


Figure 1. The NIRSpect/G395H white light curves (left) for L168-9b from the Aesop (top), Tiberius (middle), and Eureka! (bottom) reductions for visits 1 (pink), 2 (blue), and 3 (green), compared to the best-fitting transit+systematics models (black). The residuals for each visit are shown in the right panel.

We first fit the broadband NRS1 and NRS2 white light curves for each visit by fixing the period, P , to the value in [Astudillo-Defru et al. \(2020\)](#), setting the eccentricity, e , to zero and argument of periastron, ω , to ninety, and fitting for the mid-transit time, T_0 , the scaled semi-major axis, a/R_\star , inclination, i , planet-to-star radius ratio, R_p/R_\star , and stellar baseline flux using wide uniform priors. For the spectroscopic light curves, we fixed T_0 , a/R_\star , and i to the best-fit values from the broadband light curves (presented in Table 2) and fit for R_p/R_\star . We adopted the optimized parameters and their standard deviations as the best-fitting value and associated uncertainty for our fitted parameters. We held the non-linear limb-darkening coefficients ([Claret 2000](#)) fixed to theoretical values, which we computed using ExoTiC-LD ([Grant & Wakeford 2022](#)) with Set One of the MPS-ATLAS stellar models ([Kostogryz et al. 2022, 2023](#)) and the stellar effective temperature T_{eff} , surface gravity $\log(g)$, and metallicity $[\text{Fe}/\text{H}]_\star$ values given in Table 1. The **Aesop** best-fit white light curves and residuals for each visit are shown in the top panel of Figure 1.

3.1.2. *Tiberius*

We used the **Tiberius** pipeline, which builds upon the LRG-BEASTS spectral reduction and analysis pipelines introduced in [Kirk et al. \(2018, 2019, 2021\)](#), to provide an independent reduction of the data to ensure consistency and robust conclusions. We began our data reduction with our custom group-level background subtracted products from **Tiberius** Stage 1. For each detector, we created bad-pixel masks by manually identifying hot pixels within the data. We then included 5σ outlier pixels in the mask, which were identified via running medians operating along the pixel rows. Custom saturated pixel masks were created by flagging a column as saturated if any pixel within that column was saturated for any integration. Prior to identifying the spectral trace, we interpolated each column of the detectors onto a grid $10\times$ finer than the initial spatial resolution. This step reduces the noise in the extracted data by improving the extraction of flux at the sub-pixel level, particularly where the edges of the photometric aperture bisect a pixel. We also interpolated over the bad pixels using their nearest neighboring pixels in x and y .

We traced the spectra by fitting Gaussians at each column and used a median filter, calculated with a moving box with a width of five pixels in the finely interpolated data, to smooth the measured centers of the trace. We fitted these smoothed centers with a 4th-order polynomial, removed points that deviated from the median by 5σ , and re-fitted with a 4th-order poly-

nomial. To remove residual background flux not captured by the group-level destriping, we first fit a linear polynomial along each column. We then masked the stellar spectrum, where the mask is defined by an aperture with a width of ten pixels centered on the trace. We also masked an additional four pixels on either side of the aperture so that the background was not fitting the wings of the stellar PSF, and we clipped any pixels within the background that deviated by more than three standard deviations from the mean for that particular column and frame. After removing the background in each column, the stellar spectra were then extracted by summing within the 10-pixel wide aperture and correcting for pixel oversampling caused by the interpolation onto a finer grid, as described above. The uncertainties in the stellar spectra were calculated from the photon noise and read noise.

With the broadband light curves (NRS1: 2.86–3.69 μm , NRS2: 3.82–5.06 μm) generated from the **Tiberius** stellar spectra, we fitted for R_p/R_\star , i , T_0 , a/R_\star , the quadratic limb darkening coefficient u_1 , and the coefficients of the systematics model parameters (x and y pixel shifts, FWHM, and background), with P , e , and fixed to the values given in Table 1 and u_2 fixed. We used uniform priors for all the fitted parameters. Our analytic transit light-curve model was generated with **batman** ([Kreidberg 2015](#)). We fit our broadband light curves with a transit+systematics model using the Levenberg Marquardt algorithm and assuming a linear polynomial function for each systematic being fit. For the 60 pixel spectroscopic light curves, we held a/R_\star , i , and T_0 fixed to the best-fit values from the broadband light curve fits (Table 2). We then fit the spectroscopic light curves, again using the Levenberg-Marquardt algorithm with linear polynomial functions for the same systematics detrending parameters detailed above. We used wide uniform priors for all fitted parameters. The **Tiberius** fitted white light curves and residuals are shown in the middle panel of Figure 1, and the best-fit white light curve parameters are shown in Table 2.

3.1.3. *Eureka!*

We also used **Eureka!**¹ (version 0.10; [Bell et al. 2022](#)) to provide an additional independent reduction of our observations, treating the data from NRS1 and NRS2 separately throughout our analysis. For Stages 1 and 2 (which follow the standard steps of the first two stages of the **jwst** pipeline version 1.11.4; [Bushouse et al. 2022](#)), we used the default **Eureka!** parameters, a jump detection threshold of 15, and the custom $1/f$ noise correc-

¹ <https://github.com/kevin218/Eureka>

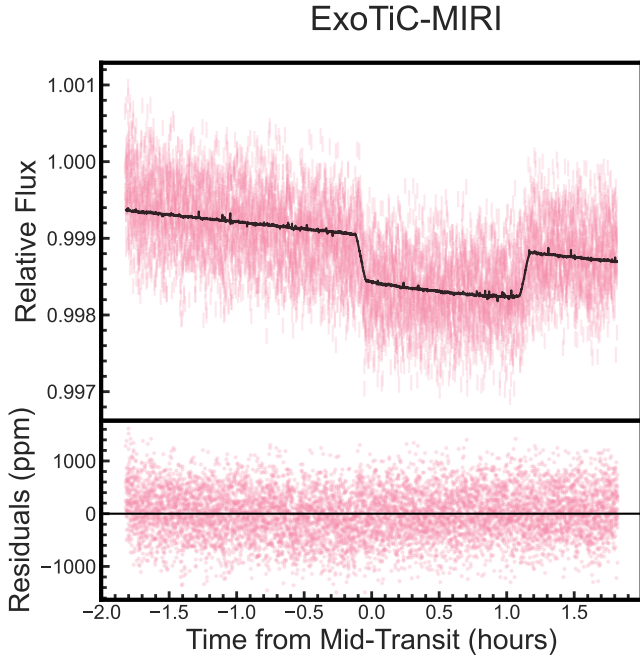


Figure 2. The MIRI/LRS white light curve for L168-9b (points) compared to the best-fitting transit+systematics model (black). The residuals are shown in the bottom panel.

tion method from ExoTiC-JEDI² (which leads to fewer temporal outliers).

We then ran *Eureka!* Stage 3 to extract the time-series stellar spectra and generate white and spectroscopic light curves for each visit. We tested combinations of extraction apertures of 4-8 pixels from the center of the flattened spectral trace, background apertures of 8-11 pixels, and sigma thresholds for optimal extraction outlier rejection of 10 and 60, and two different background subtraction methods (an additional column-by-column mean subtraction and a full frame median subtraction). For each detector and each visit, we selected the combination of reduction parameters that minimizes the RMS scatter in the resulting white light curves. For NRS1, we used aperture half-widths of 4, 6, and 4 and background apertures of 8, 9, and 10, for visits 1, 2, and 3, respectively. For NRS2, we used aperture half-widths of 4, 5, and 4 for visits 1, 2, and 3, respectively and background apertures of 8 for all visits. We used an additional column-by-column background subtraction for NRS1 visits 1 and 2, and a full frame background subtraction for NRS1 visit 3 as well as all visits of NRS2. We selected a 10σ threshold for the optimal extraction of NRS1 for visits 2 and 3 and both detectors in visit 1.

² <https://github.com/Exo-TiC/ExoTiC-JEDI>

We also selected a 60σ threshold for the optimal extraction of visits 2 and 3 for NRS2.

From our white and 60 pixel spectroscopic light curves, we iteratively trimmed 3σ outliers three times from a 50 point rolling median in time. We then used *emcee* (Foreman-Mackey et al. 2013) to fit a combined transit+systematics model to the light curves, fitting for i , a/R_\star , T_0 , and R_p/R_\star . The transit model was generated using *batman* (Kreidberg 2015), and we fixed the quadratic limb-darkening coefficients to the theoretical values computed with ExoTiC-LD (Grant & Wakeford 2022) using the stellar parameters given in Table 1 and Set One of the MPS-ATLAS models (Kostogryz et al. 2022, 2023). Our instrumental noise model, S , was of the form

$$S = p_1 + p_2 \times T + p_3 \times X + p_4 \times Y, \quad (2)$$

where p_N is a parameter fitted for in our instrumental noise model, T is the vector of times, and X and Y are vectors of the positions of the trace from *Eureka!* Stage 3. We trimmed the first 500 points (30 minutes) to remove any initial ramp. We initialized $3\times$ the number of free parameters as the number of walkers and used a burn-in of 50,000 steps (which is discarded), followed by a production run of 50,000 steps to ensure adequate sampling of the posterior. The fitted white light curves and residuals are shown in the bottom panel of Figure 1, and the best-fitting parameters are given in Table 2.

For the spectroscopic light curve fits, we combined the MCMC chains from the NRS1 and NRS2 fits for i , a/R_\star , and T_0 . We used the resulting chains as strong Gaussian priors for these parameters centered at the median of each combined chain and with a conservative width of three times the standard deviation of the combined chains. We utilized a wide flat prior for R_p/R_\star for each spectroscopic bin. We also jointly fit the three visits for each detector in the same manner described above, but assuming a common i , a/R_\star , T_0 , and R_p/R_\star for all three visits.

3.2. MIRI LRS

3.2.1. ExoTiC-MIRI

We reduced the commissioning observations of L 168-9b using the ExoTiC-MIRI³ pipeline (Grant et al. 2023). We began with the uncalibrated files from the *jwst* pipeline (version 1.8.2, context map 1078; Bushouse et al. 2022). We then processed the data using the standard Stage 1 steps for time-series observations, as well as custom steps unique to the ExoTiC-MIRI pipeline. We

³ <https://exotic-miri.readthedocs.io/en/latest/>

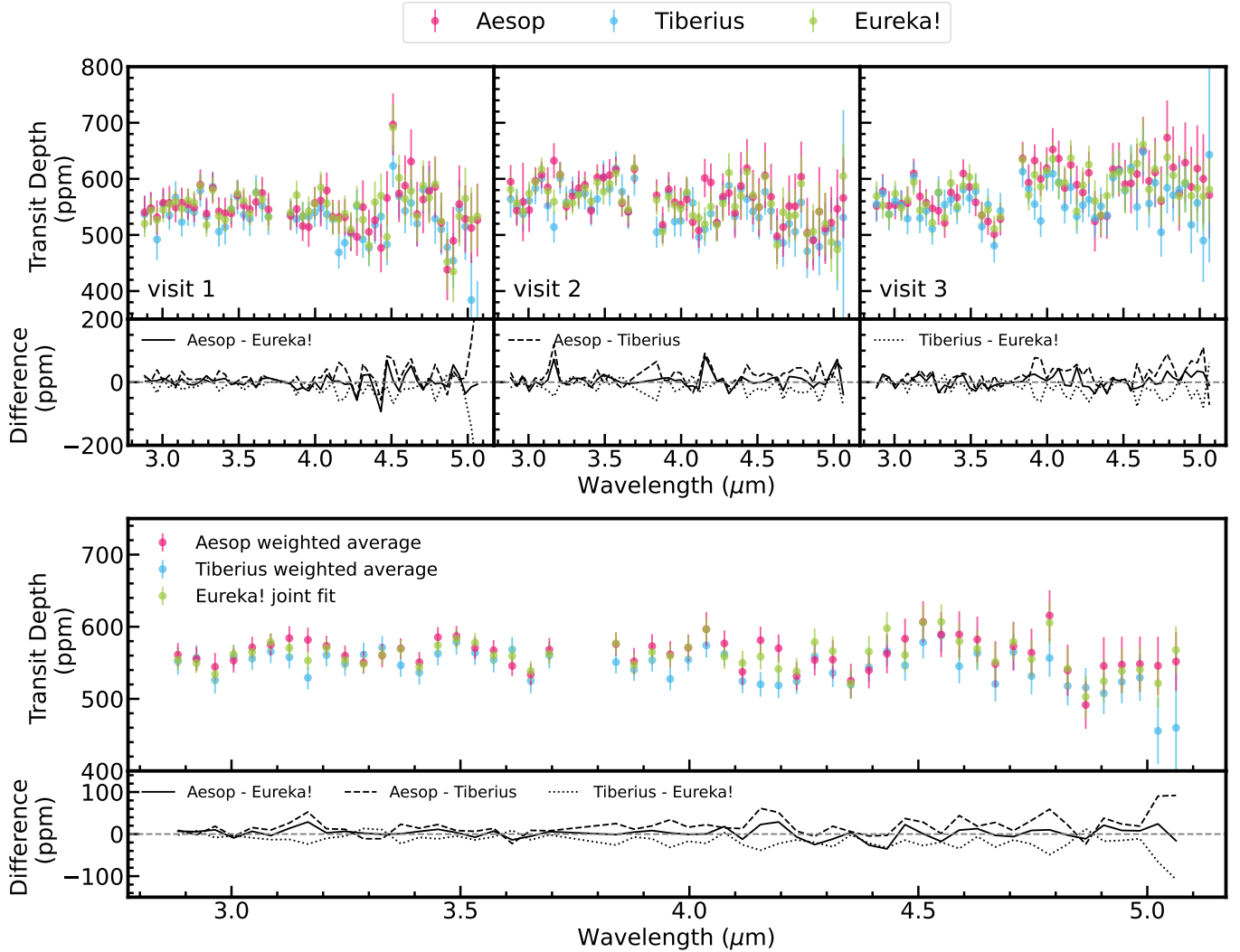


Figure 3. *Top:* Comparison of the *Aesop* (pink), *Tiberius* (blue), and *Eureka!* (green) reductions for visit 1 (left), visit 2 (middle), and visit 3 (left). *Bottom:* the combined transmission spectrum for all three visits from the *Aesop* and *Tiberius* weighted averages and the *Eureka!* joint fit.

started with the data quality initialization step, followed by corrections for saturation, linearity, and dark current. We applied the `custom_drop_groups` step to drop the first five groups before the linearity correction, since these groups may adversely affect the group-level ramps due to detector effects such as reset switch charge decay as well as the last frame effect pulling down the final group (Ressler et al. 2015; Wright et al. 2023). For the jump step, we set the detection threshold to 15 to prevent spurious cosmic ray flagging. We then proceeded with the standard ramp fitting and gain scale correction steps, where we set the gain value to 3.1 electrons per data number (Bell et al. 2023).

In Stage 2, we processed the `rateints` files with the standard flat fielding step, and applied custom cleaning and background subtraction routines. The custom

cleaning step replaced known bad pixels and removed unidentified outliers from the data quality arrays by estimating a spatial profile from polynomial fits to the detector columns and iteratively replacing pixels by the profile value if they were flagged as `DO_NOT_USE` or were more than 4σ discrepant. In the custom background step, we subtracted a row-by-row background using the median value from columns 8 to 17 and 56 to 72. We then performed the spectral extraction using a fixed-width box aperture centered on column 36 and extended four pixels to the left and right to obtain the time-series stellar spectra.

We extracted the broadband MIRI/LRS light curve by summing up the stellar flux in the time-series between 4.785 and 11.935 μm . For the spectroscopic light curves, we generated 48 wavelength bins $\sim 0.15 \mu\text{m}$ wide

Table 2. White light curve best-fit values for the *Aesop*, *Tiberius*, *Eureka!*, and *ExoTiC-MIRI* reductions, as well as the *Eureka!* joint fit.

			T_0 (MJD)	a/R_\star	i ($^\circ$)	R_p/R_\star
Aesop	visit 1	NRS1	$60098.46289 \pm 5e-5$	8.58 ± 0.80	88.32 ± 1.34	0.02381 ± 0.00017
		NRS2	$60098.46279 \pm 1e-4$	7.06 ± 0.10	85.00 ± 1.01	0.02395 ± 0.00020
	visit 2	NRS1	$60113.87973 \pm 4e-5$	7.86 ± 0.89	89.44 ± 2.51	0.02418 ± 0.00017
		NRS2	$60113.87952 \pm 7e-5$	8.66 ± 0.17	88.32 ± 2.68	0.02316 ± 0.00019
	visit 3	NRS1	$60122.28873 \pm 6e-5$	7.21 ± 0.82	85.31 ± 2.28	0.02429 ± 0.00016
		NRS2	$60122.28909 \pm 6e-5$	7.72 ± 0.15	85.76 ± 2.08	0.02439 ± 0.00019
Tiberius	visit 1	NRS1	$60098.46294 \pm 1e-4$	8.25 ± 0.79	87.66 ± 2.20	0.02343 ± 0.00030
		NRS2	$60098.46300 \pm 2e-4$	7.11 ± 0.76	85.08 ± 1.59	0.02353 ± 0.00031
	visit 2	NRS1	$60113.87997 \pm 1e-4$	7.52 ± 0.63	85.93 ± 1.34	0.02416 ± 0.00029
		NRS2	$60113.87968 \pm 2e-4$	8.28 ± 0.91	87.73 ± 2.57	0.02371 ± 0.00018
	visit 3	NRS1	$60122.28912 \pm 2e-4$	6.93 ± 0.56	84.72 ± 1.16	0.02363 ± 0.00029
		NRS2	$60122.28935 \pm 2e-4$	7.03 ± 0.64	84.91 ± 1.32	0.02491 ± 0.00033
Eureka!	visit 1	NRS1	$60098.46286 \pm 5e-5$	8.71 ± 0.40	89.33 ± 1.73	0.02348 ± 0.00016
		NRS2	$60098.46270 \pm 8e-5$	8.28 ± 0.58	87.44 ± 2.04	0.02344 ± 0.00020
	visit 2	NRS1	$60113.87982 \pm 6e-5$	8.58 ± 0.46	88.74 ± 1.92	0.02409 ± 0.00018
		NRS2	$60113.87960 \pm 6e-5$	8.76 ± 0.34	89.40 ± 1.58	0.02346 ± 0.00016
	visit 3	NRS1	$60122.28884 \pm 6e-5$	8.20 ± 0.60	87.26 ± 2.02	0.02369 ± 0.00022
		NRS2	$60122.28894 \pm 7e-5$	8.01 ± 0.60	86.86 ± 1.97	0.02455 ± 0.00020
Eureka! joint fit	all visits	NRS1	$60098.46292 \pm 4e-5$	8.39 ± 0.47	87.74 ± 1.61	0.02379 ± 0.00015
			$60113.87972 \pm 4e-5$			
			$60122.28888 \pm 4e-5$			
		NRS2	$60098.46284 \pm 4e-5$	8.72 ± 0.30	89.43 ± 1.55	0.02358 ± 0.00028
			$60113.87964 \pm 4e-5$			
	$60122.28880 \pm 4e-5$					
ExoTiC-MIRI	visit 1	LRS	$59082.85642 \pm 8e-5$	8.24 ± 0.64	88.1 ± 1.25	0.02333 ± 0.00028

following the binning scheme of [Bouwman et al. \(2023\)](#). We iteratively removed points in the white and spectroscopic light curves that were 4σ outliers in the residuals, and trimmed the first 1126 integrations (~ 30 minutes) in the time-series to remove the detector settling ramp. We then fit each light curve with a transit model generated using *batman* multiplied by a systematics model of the form:

$$S(\lambda) = c_0 + (c_1 \times x) + (c_2 \times y) + (c_3 \times t) \quad (3)$$

where x and y are the x - and y - pixel positional shifts on the detector, t is time, and the coefficients c_0 , c_1 , and c_2 are constants to be fit.

We then fit the broadband LRS white light curve using a least-squares minimizer. We fixed P to the [Astudillo-Defru et al. \(2020\)](#) value, setting e to zero and ω to ninety, and fit for T_0 , a/R_\star , i , and R_p/R_\star using wide uniform priors. We adopted the optimized parameters and their standard deviations as the best-fit white light curve values, which are given in Table 2. For the spectroscopic light curve fits, we fixed T_0 , a/R_\star , and i to best-

fit values from the white light curves, and fit for R_p/R_\star . We fixed the quadratic limb darkening coefficients to the theoretical values calculated using *ExoTiC-LD* ([Grant & Wakeford 2022](#)) and Set One of the MPS-ATLAS stellar models ([Kostogryz et al. 2022, 2023](#)) and the stellar T_{eff} , $\log(g)$, and $[\text{Fe}/\text{H}]_\star$ given in Table 1. The fitted *ExoTiC-MIRI* white light curve and residuals is shown in Figure 2.

4. INTERPRETATION OF L 168-9 b's TRANSMISSION SPECTRUM

The 3-5 μm transmission spectrum using a 60 pixel binning scheme for L 168-9 b from *NIRSpec/G395H* for all three visits and all three reductions are shown in the top panels of Figure 3. Each visit is generally consistent across the three independent reductions, with a median difference in transit depth of 42 ppm across visits for the *Aesop* reduction (compared to the median transit depth uncertainty of 35 ppm), 39 ppm for the *Tiberius* reduction (median transit depth uncertainty of 54 ppm), and 41 ppm for the *Eureka!* reduction (median transit depth uncertainty of 29 ppm). We do not apply any off-

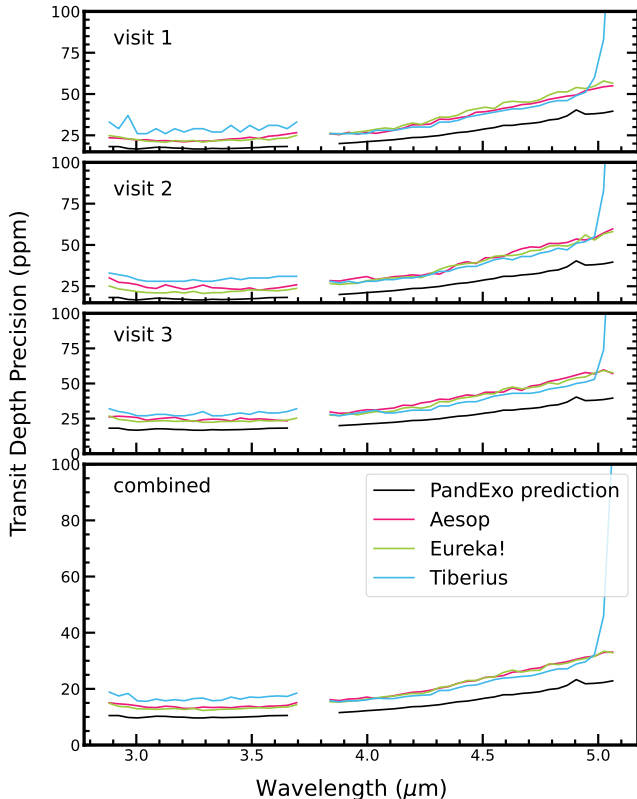


Figure 4. The transit depth precisions achieved by each independent reduction compared to the predicted values from **PandExo** simulations for each individual visit and for the combined spectra from each reduction.

sets between the NRS1 and NRS2 detectors, although we note a median offset of 49 ppm between NRS1 and NRS2 in visit 3 across all three reductions. Across visits, the three reductions are also similar, with a median difference between the **Aesop** and **Eureka!** reductions of 18 ppm, 26 ppm, and 19 ppm for visits 1, 2, and 3, respectively. The **Aesop** and **Tiberius** reductions have a median difference of 21 ppm, 22 ppm, and 26 ppm for the three visits, whereas the median transit depth difference between the **Tiberius** and **Eureka!** reductions is 23 ppm, 34 ppm, and 26 ppm.

The combined spectra for each reduction (the weighted average of the three visits for the **Aesop** and **Tiberius** reductions, as well as the **Eureka!** joint fit) are shown in the bottom panel of Figure 3. No offsets have been applied to the combined spectra. The median transit depth uncertainties for the **Aesop** weighted average, **Tiberius** weighted average, and **Eureka!** joint fit are 20 ppm, 28 ppm, and 18 ppm, respectively. Taken together, the reductions are consistent within the uncertainties with a median transit depth difference of 10 ppm between the **Aesop** and **Eureka!** reductions, 12 ppm between **Aesop** and **Tiberius**, and 15 ppm between the

Tiberius and **Eureka!** reductions. We also compare the transit depth precisions from each independent reduction to the predicted precisions from **PandExo** simulations in Figure 4. Despite the fact that the three reductions are comparable, none of them achieve the precisions predicted from the **PandExo** simulations across all NRS1 and NRS2 wavelengths. On average, the **Aesop**, **Tiberius**, and **Eureka!** reductions are $1.4\times$, $2.2\times$, and $1.3\times$ the **PandExo** value for each visit and $1.3\times$, $2.1\times$, and $1.2\times$ the **PandExo** value for the combined spectra.

The precisions achieved by our **ExoTiC-MIRI** reduction are comparable to the **Eureka!** and **CASCADE** reductions reported in **Bouwman et al. (2023)**, as shown in Figure 6. The mid-infrared transmission spectra extracted using **ExoTiC-MIRI**, **Eureka!**, and **CASCADE** are $1.7\times$, $1.7\times$, and $1.8\times$ the predicted value from **PandExo** simulations, respectively.

None of the individual **NIRSpec/G395H** visits across the three independent reductions show evidence of gaseous molecular absorption features. Our spectrum from the reduction of the **MIRI/LRS** commissioning observations is shown in Figure 5, which also appears to be featureless albeit with larger uncertainties. We consider the near-infrared **NIRSpec/G395H** spectrum as well as the combined near- to mid-infrared **NIRSpec/G395H+MIRI/LRS** transmission spectrum in our interpretation of this planet’s atmospheric properties (§4.1).

4.1. Forward Model Fits

We produced a small grid of atmospheric models to interpret the measured transmission spectrum of L 168-9 b and quantify the part of parameter space ruled out by our data, as in previous papers in this program (**Alderson et al. 2024**; **Wallack et al. 2024**; **Scarsdale et al. 2024, submitted**). Briefly, we consider the 5-parameter double-gray analytical temperature-pressure profile of **Guillot (2010)**, with which we generated atmospheric abundance profiles using the chemical equilibrium grid from **Line et al. (2013)**⁴ calculated using **NASA CEA (Gordon & McBride 1994)**. We included abundances for H_2O , CH_4 , CO , CO_2 , NH_3 , N_2 , HCN , H_2S , PH_3 , C_2H_2 , C_2H_6 , Na , K , TiO , VO , Fe , H , H_2 , and He . We varied the atmospheric metallicity from 0.01 to $1000\times$ solar and fixed the C/O to solar (0.55; **Asplund et al. 2009**). A cloud deck with a total optical depth of 10 is included in the model to represent the opaque pressure level, which could be due to gray aerosols or the solid surface of the planet that prevent us from probing

⁴ <https://github.com/mrline/CHIMERA>

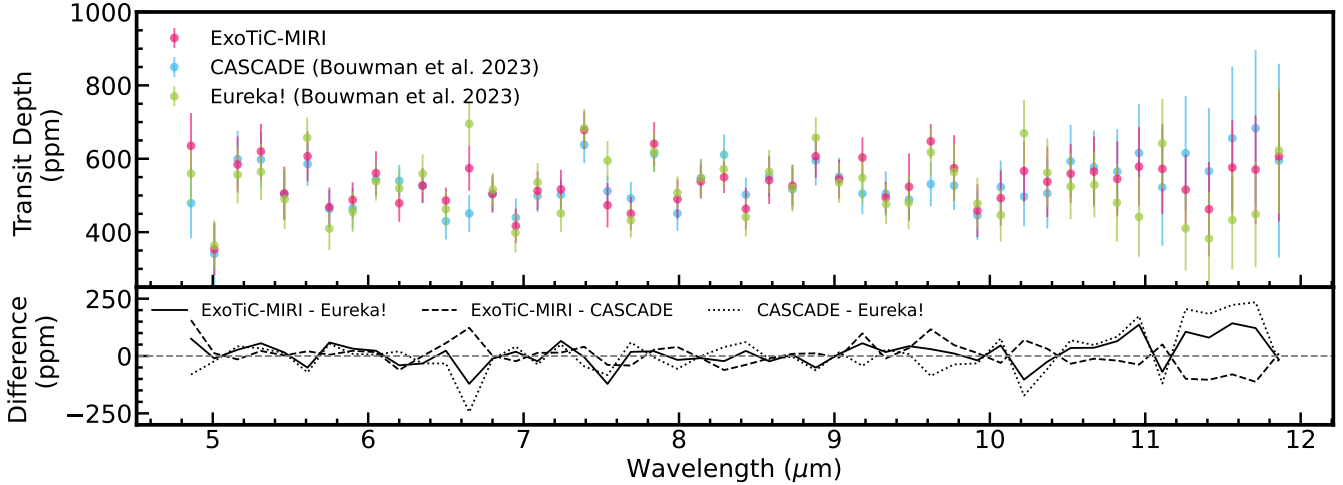


Figure 5. *Top:* Comparison of the ExoTiC-MIRI (pink) reduction of the MIRI/LRS commissioning data compared to the CASCADE (blue) and Eureka! (green) reductions from Bouwman et al. (2023).

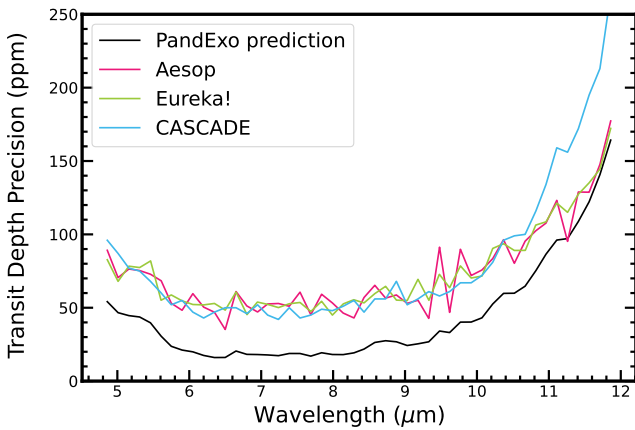


Figure 6. The MIRI transit depth precisions for each independent reduction compared to the predictions from PandExo.

deeper pressures. The base of the cloud is set to 10 bars, with the cloud top pressure varying from 1 to 10^{-4} bars. We generated spectra from these atmospheric models using the open-source atmospheric modeling code PICASO⁵ (Batalha et al. 2019; Mukherjee et al. 2023), with opacities from Batalha et al. (2020) for a subset of the above list of species (Na, K, CH₄, CO, CO₂, H₂O, H₂S, NH₃, PH₃, TiO, and VO). The spectral resolution of the opacities are sufficient for fitting to the R \sim 100 final observed transmission spectra. In addition to the model grid, we also generated several “end-member” atmospheric models consisting of single gases (CH₄, H₂O, and CO₂), for which we assumed an isothermal temperature profile set to the equilibrium temperature of the planet assuming

zero albedo and full heat redistribution ($T_{\text{eq}}=981$ K). Finally, we considered a flat line model to represent a high altitude gray cloud or the lack of an atmosphere.

We fitted the aforementioned models to the near-infrared NIRSpec/G395H (3–5 μm) transmission spectrum only, as well as to the full NIRSpec/G395H+MIRI/LRS (3–12 μm) spectrum by optimizing the vertical offsets of the model spectra. The number of degrees of freedom for each model is constant and computed as $n - m$, where n is the number of data points ($n=54$ for the G395H-only fits and $n=102$ for the G395H+MIRI fits) and $m=1$ is the number of fitted parameters (vertical offset). For the G395H+MIRI fits, we shifted the MIRI data vertically by 29 ppm such that the mean transit depth across the MIRI wavelengths matched that of the G395H data. From our fits, we quantified our model selection by computing the χ^2 statistic. The results of our model fitting exercises are shown in Table 3. Henceforth in the paper, we focus on the Aesop weighted average spectrum in our interpretation of L 168-9 b’s atmosphere, since we demonstrated in Section 4 that all of the independent reductions presented here are consistent within 1σ .

The Aesop weighted average G395H and G395H+MIRI transmission spectra of L 168-9 b compared to the single-gas and flat models, as well as several illuminating models from the model grid ($1\times$, $25\times$, and $100\times$ solar with opaque pressure levels at 1 bar) are shown in Figure 7. In addition, we computed the typical size of spectral features (~ 5 scale heights; Seager & Sasselov 2000) as a function of atmospheric mean molecular weight for comparison to the data using Equation 1 from Stevenson (2016). We find that both datasets prefer the single gas models and the flat model over any of the su-

⁵ <https://github.com/natashabatalha/picaso>

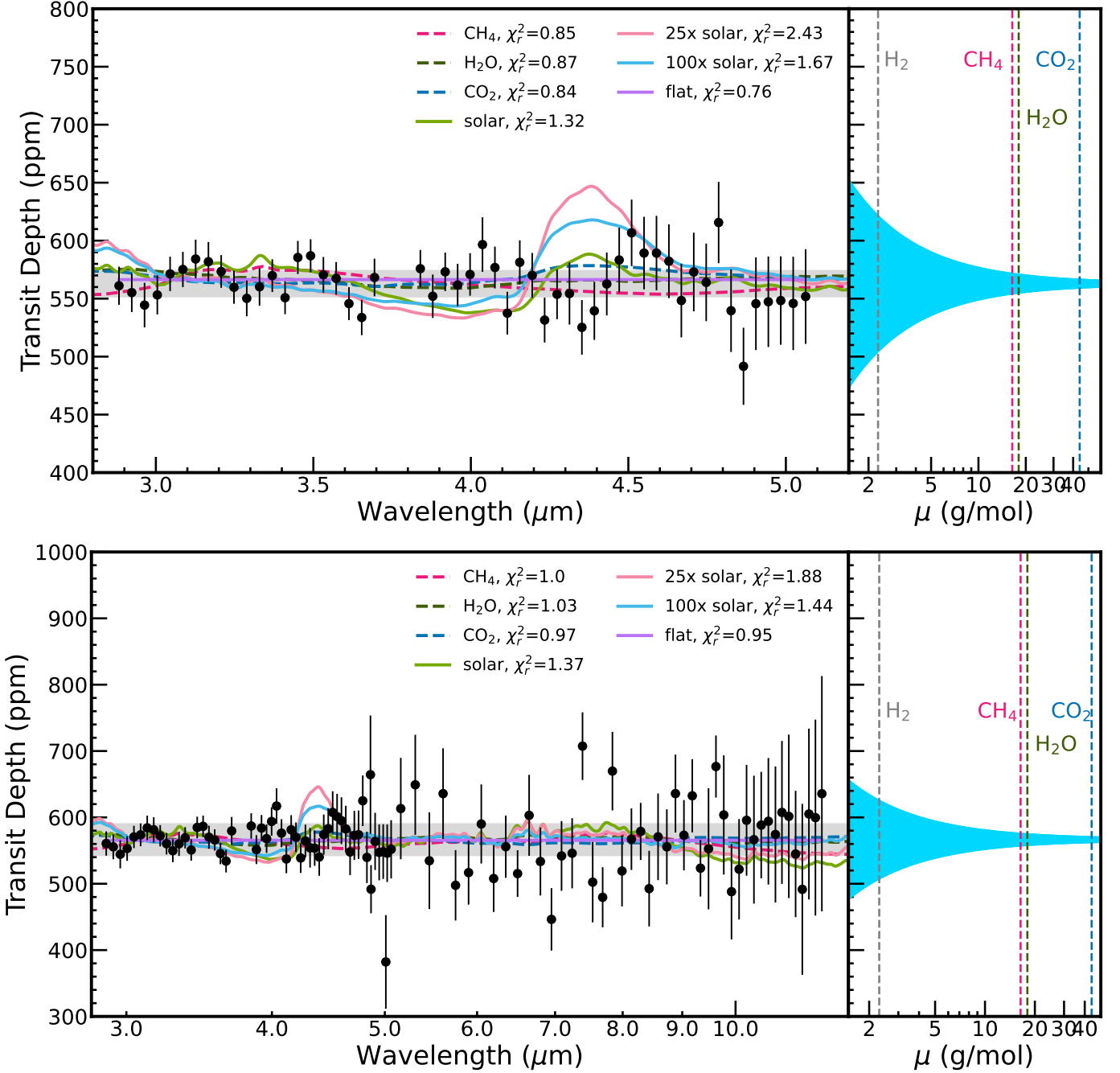


Figure 7. *Top:* Left: The *Aesop* weighted average NIRSpect/G395H transmission spectrum (black points) of L 168-9 b compared to 1D isothermal atmospheric models assuming single gas compositions, with methane (dark pink, dashed), water (dark green, dashed), and carbon dioxide (dark blue, dashed), as well as solar composition (light green), 25 \times solar metallicity (light pink), and 100 \times solar (light blue) models extracted from the model grid generated using the analytical TP profile from Guillot (2010). A flat line model is shown in purple. The best-fitting ($\chi_r=0.76$) atmospheric model is the flat line model, consistent with either a high-altitude gray cloud deck, atmospheres with mean molecular weights greater than 4 g mol⁻¹, or no atmosphere. The light gray shaded region corresponds to the 1σ scatter in the data. Right: Typical size of spectral features (± 5 atmospheric scale heights; Seager & Sasselov 2000) as a function of mean molecular weight (MMW) compared to the MMW of molecular hydrogen (2.3 g/mol; gray), methane (16.0 g/mol; pink), water (18.02 g/mol; green), and carbon dioxide (44.01 g/mol; blue). The transit depth uncertainty per spectral bin as well as the scatter in the transmission spectrum far exceeds the scale height of any possible high mean molecular weight atmosphere for this planet. *Bottom:* The same as the top panel, except for the NIRSpect/G395H (*Aesop* weighted average) + MIRI/LRS transmission spectrum. A flat line best fits the near- to mid-infrared transmission spectrum ($\chi_r^2=0.95$).

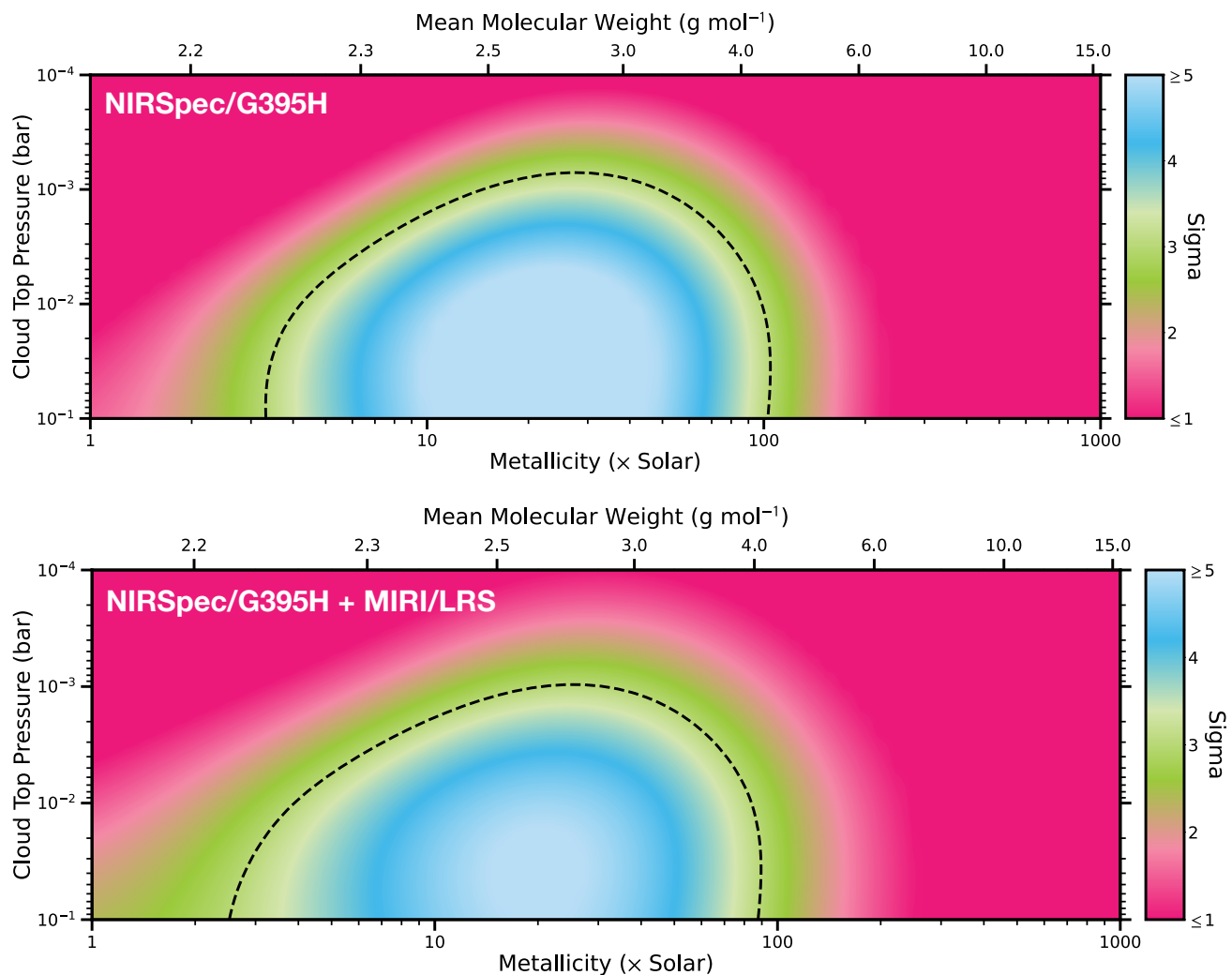


Figure 8. *Top:* Cloud top pressure versus atmospheric metallicity for the *Aesop* weighted average NIRSpect/G395H transmission spectrum of L 168-9b, where the colored contours correspond to the significance level (in σ) to which we can rule out our forward models. The dashed black curve indicates the threshold beyond which we can rule out regions of this parameter space to $>3\sigma$ confidence. *Bottom:* Same as the top panel, but for the NIRSpect/G395H+MIRI/LRS transmission spectrum of L 168-9b.

Table 3. Reduced chi-squared χ_r^2 values from the forward model fits described in Section 4.1.

		CH ₄	CO ₂	H ₂ O	1× solar	25× solar	100× solar	flat
G395H visit 1	Aesop	0.54	0.62	0.58	0.66	1.21	0.93	0.57
	Tiberius	0.68	0.62	0.78	0.92	1.26	1.00	0.71
	Eureka!	0.82	0.86	0.83	1.16	1.98	1.56	0.76
G395H visit 2	Aesop	0.83	0.89	0.89	0.86	1.22	1.01	0.88
	Tiberius	0.38	0.41	0.40	1.48	1.53	1.45	0.40
	Eureka!	1.17	1.13	1.18	1.07	2.02	1.78	1.07
G395H visit 3	Aesop	1.34	1.13	1.24	1.73	1.78	1.45	1.14
	Tiberius	0.86	0.88	0.87	1.26	1.23	1.03	0.87
	Eureka!	1.36	1.42	1.21	1.93	2.02	1.57	0.88
G395H combined	Aesop	0.85	0.87	0.84	1.29	2.42	1.67	0.76
	Tiberius	0.86	0.86	0.68	1.45	1.89	1.35	0.87
	Eureka!	1.18	1.11	1.14	1.73	3.5	2.41	1.08
G395H combined + MIRI	Aesop	1.0	1.03	0.97	1.37	1.86	1.42	0.95

per solar metallicity models, with the solar metallicity model possessing intermediate χ_r^2 , likely due to the lack of high amplitude molecular features (e.g., CO₂). This finding suggests a high (>4 g mol⁻¹) atmospheric mean molecular weight, the presence of high altitude aerosols, or the lack of an atmosphere altogether. Among the relatively well-fit models, the χ_r^2 values are all similar, and the lack of any discernible atmospheric features prevents us from discriminating between them.

Figure 8 shows the σ -significance across the opaque pressure level–metallicity parameter space given our full model grid. We compute the σ -significance from the χ_r^2 values by converting the latter to p-values and then assuming normally distributed errors on the data. We find that the transmission spectrum of L 168-9 b rules out atmospheric compositions between 2–3× and 100× solar at >3 σ , assuming high surface pressure (>1 bar), cloudless atmospheres. These metallicity bounds roughly correspond to atmospheric mean molecular weights between 2.2 and 4 g mol⁻¹. We rule out a smaller range of metallicities for lower surface pressures and/or cloudy atmospheres, such that for opaque pressure levels <1 mbar all considered metallicities are allowed. These results are in agreement with our findings using our representative models (Figure 7): at low (<2–3× solar) metallicity, the low abundance of CO₂ leads to relatively low amplitude spectral features dominated by the broad CH₄ band centered at 3.3 μ m; at high (>100× solar) metallicity, the increased atmospheric mean molecular weight reduces spectral amplitudes across all features; at intermediate metallicities, the relatively low atmospheric mean molecular weight coupled with the higher CO₂ abundances leads to the appearance of the large CO₂ band at 4.3 μ m, which rises above the scatter of the data, requiring high altitude clouds to flatten the

model to produce a good fit. In general we see similar results between the G395H-only and G395H+MIRI cases, except that the latter dataset is able to rule out more of the lower metallicity portion of parameter space (Figure 8). This is likely due to the large amplitude decrease in the transit depth redward of 9 μ m caused by the lack of significant molecular opacity there.

5. DISCUSSION

5.1. An Emerging Trend for Rocky Exoplanets

The featureless transmission spectrum of L 168-9 b joins a growing number of similar rocky exoplanet observations with JWST (TRAPPIST-1b, Lim et al. 2023; LHS 475b, Lustig-Yaeger & Fu et al. 2023; GH 1132b, May & MacDonald et al. 2023; GJ 486b, Moran & Stevenson et al. 2023; TOI 836b, Alderson et al. 2024; GJ 341b, Kirk et al. 2024; L98-59c, Scarsdale et al. 2024, submitted). As with this work, these studies largely conclude that their planets likely have either high mean molecular weight atmospheres, high altitude aerosols, or no atmospheres at all. Complementing these transmission studies are emission observations of rocky exoplanet daysides and/or full-orbit thermal phase curves by the Spitzer Space Telescope (LHS 3844b, Kreidberg et al. 2019) and JWST (TRAPPIST-1b, Greene et al. 2023; TRAPPIST-1c, Zieba et al. 2023; GJ 367b, Zhang et al. 2024b; 55 Cnc e, Hu et al. 2024), many of which suggest the lack of thick atmospheres capable of redistributing heat from the dayside to the nightside. All but one of these planets (55 Cnc e) orbit M dwarfs, which have high activity levels and bright, prolonged pre-main sequence phases (Luger & Barnes 2015; Schaefer et al. 2016; Krissansen-Totton & Fortney 2022). The lack of spectral features in either emission or transmission has therefore been in-

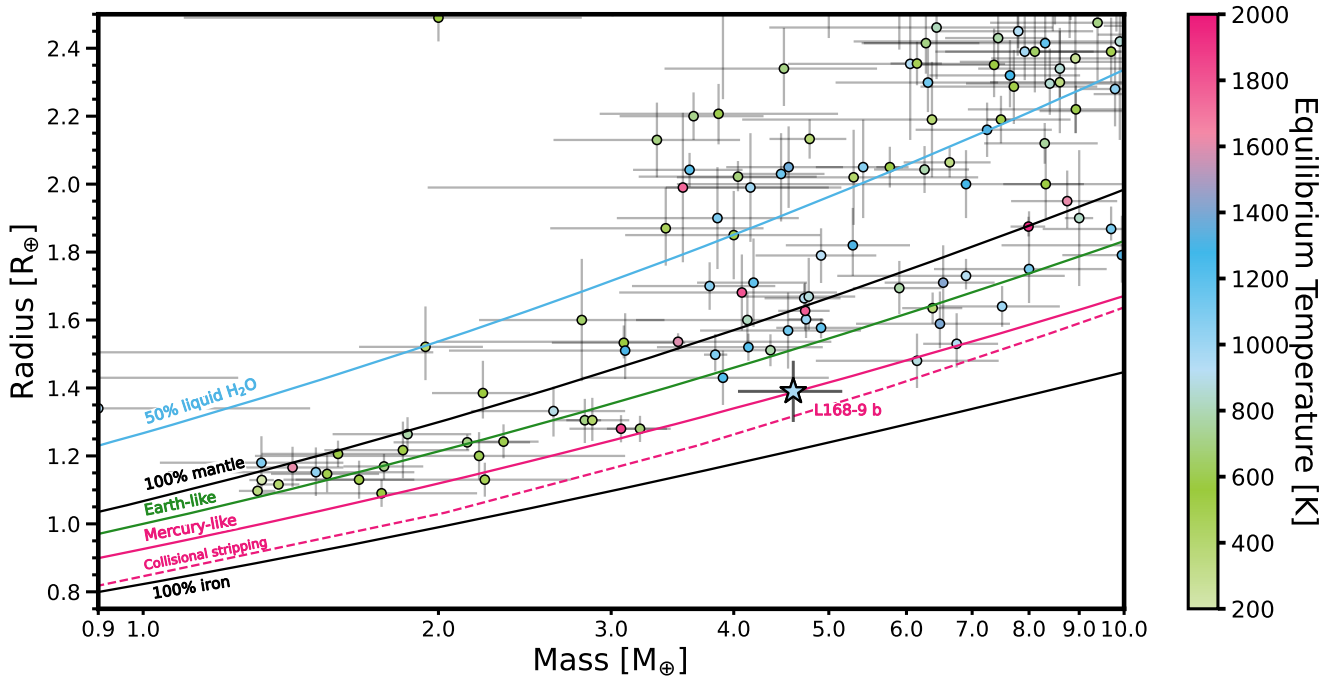


Figure 9. Mass-radius diagram for small planets (points) color coded by planetary equilibrium temperature compared to theoretical curves of constant composition (solid lines Zeng et al. 2016). The pink dashed line represents the smallest radius a rocky planet can have due to loss of its mantle by collisional stripping by planetesimals, based on the model of Marcus et al. (2010). The measured mass and radius of L168-9 b are consistent with a Mercury-like bulk composition.

terpreted as the result of catastrophic stripping of light atmospheric gases (e.g., H_2/He) from these planets by their active host stars. After this process, high mean molecular weight atmospheres remain or no significant atmospheres at all.

5.2. Photoevaporation Modeling

Our results for L168-9 b stand out from previous works in that our data allows for near-solar metallicity atmospheres (Figure 8). However, L168-9 b’s high bulk density – greater than that of Earth (see Figure 9) – likely rules out any significant low mean molecular weight envelope. In addition, the high irradiation level of the planet is likely to result in very short lifetimes for light gases. To quantify this, we ran atmospheric escape models based on the Rogers & Owen (2021) photoevaporation model. We simulated planets with a core mass of $4.6 M_\oplus$ and initial atmospheric mass fractions of 0.02, 0.05, 0.1, 0.2, 0.3, 0.5, and $1.0 \times$ the core mass. We considered the evolution of the stellar XUV flux from Owen & Wu (2017), which consists of a constant, saturated XUV flux, L_{sat} , up to the saturation time t_{sat} , followed by a power-law decrease in time:

$$L_{\text{XUV}} = \begin{cases} L_{\text{sat}} & t < t_{\text{sat}} \\ L_{\text{sat}} \left(\frac{t}{t_{\text{sat}}}\right)^{-1-a_0} & t \geq t_{\text{sat}} \end{cases} \quad (4)$$

where L_{sat} is given by

$$L_{\text{sat}} = 10^{-3.5} L_\odot \left(\frac{M_\star}{M_\odot}\right) \quad (5)$$

Following Rogers & Owen (2021), we used a t_{sat} value of 100 Myr and set a_0 to 0.5, which are the appropriate values for Sun-like stars. L_{XUV} for M dwarfs is similar to that of Sun-like stars (Shkolnik & Barman 2014), so we can appropriately adopt these values here. However, t_{sat} is longer for M dwarfs, and could reach ~ 1 Gyr (Wright et al. 2011; Pineda et al. 2021). As such, our computed envelope lifetimes are more of an upper limit. Indeed, we find that any significant primordial H_2/He atmosphere on L168-9 b should be removed within 200 Myr (as shown in Figure 10), which is far less than the estimated age of the system (~ 3 Gyr; Engle & Guinan 2023).

These results suggest that, although H_2/He -dominated atmospheres are consistent with our data (given the scatter in the transmission spectrum), it is

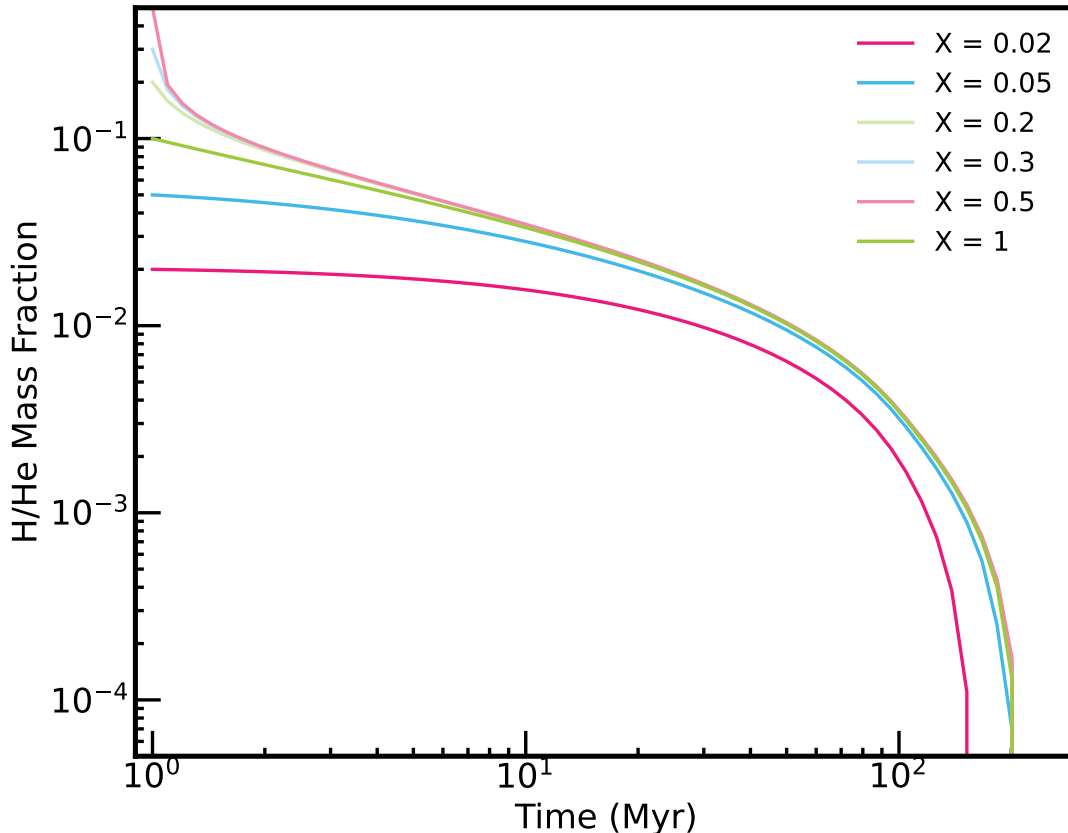


Figure 10. Photoevaporation model based on Rogers & Owen 2021, adapted to the L 168-9 system for initial H/He atmospheric mass fractions of 2% (dark pink), 5% (light pink), 20% (dark blue), 30% (light blue), 50% (dark green), and 100% (light green). For a large range of potential initial atmospheric mass fractions, L 168-9 cannot retain an atmosphere beyond the first 200 Myr of its 3 Gyr lifetime.

highly unlikely that such an atmosphere actually exists on L 168-9b. We are thus left with the possibility of either a high mean molecular weight atmosphere with or without high altitude aerosols or no atmosphere at all – consistent with previous studies of rocky exoplanets, particularly those orbiting M dwarfs.

5.3. Prospects for Future Atmospheric Characterization

Distinguishing between the high mean molecular weight atmosphere and no atmosphere scenarios for L 168-9b is the next logical step for characterizing this enigmatic world, which could shed light on its initial volatile budget, external volatile delivery rate, and outgassing history (Kane et al. 2020; Lichtenberg & Clement 2022; Krissansen-Totton 2023). To this end, secondary eclipse observations at $15\ \mu\text{m}$ with JWST/MIRI are emerging as a powerful tool to explore the presence of an atmosphere on M dwarf rocky planets (Redfield et al. 2024). We therefore explored the feasibility of $15\ \mu\text{m}$ MIRI eclipse observations for L 168-9b

for end-member atmospheric scenarios consistent with our single-gas forward models (§4.1).

We used `clima`, the 1D climate model from Wogan (2023)⁶, and the day-night heat redistribution parameterization described in Koll (2022) to estimate the day-side emission from 100 bar atmospheres composed of CO_2 , H_2O and CH_4 . The left panel of Figure 11 shows predicted P-T profiles, compared to the expected day-side emission temperature of a bare rock (1200 K), assuming a 0.1 bond albedo motivated by that of Mercury.⁷ The right panel of Figure 11 gives the resultant emission spectrum for each scenario with synthetic $15\ \mu\text{m}$ MIRI photometry observations computed with the JWST Exposure Time Calculator (Pontoppidan et al. 2016). Each synthetic data point assumes three visits, has 17 ppm precision, and ignores random

⁶ <https://github.com/Nicholaswogan/clima>

⁷ An albedo of ~ 0.19 is a plausible upper bound for a bare rock, assuming an ultramafic surface (Mansfield et al. 2019).

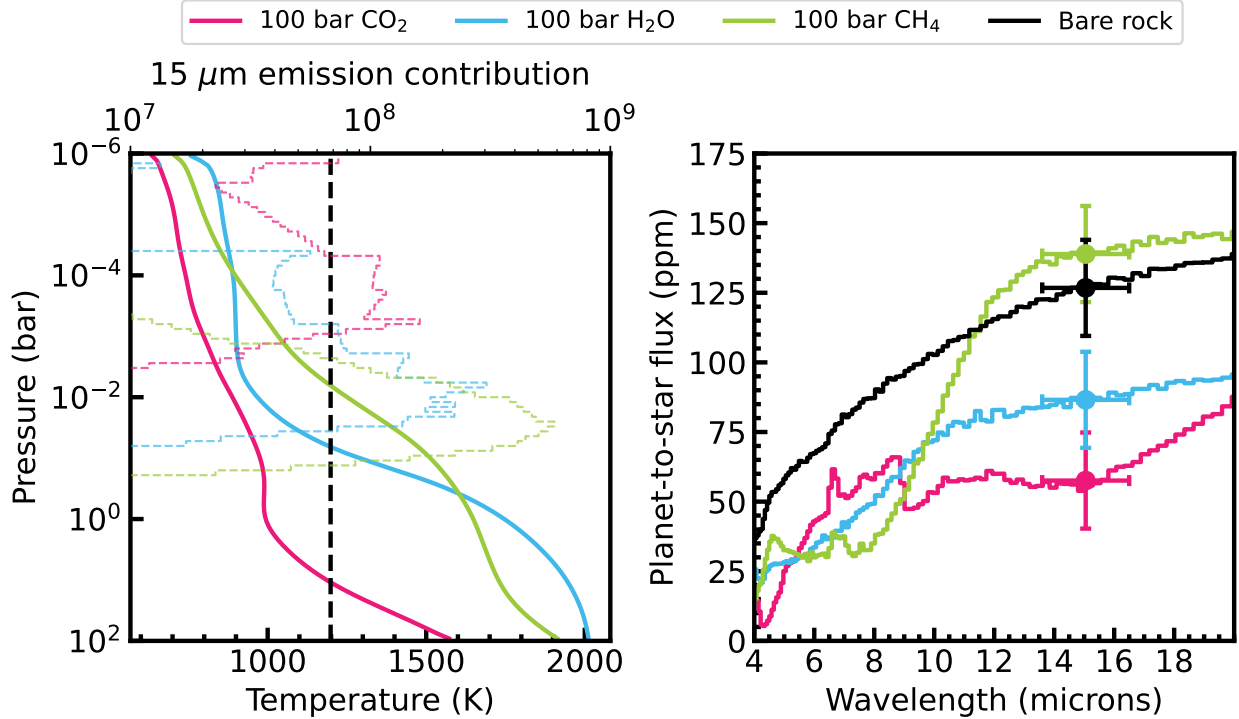


Figure 11. *Left:* Solid lines are the predicted temperature-pressure profiles from `cLima` for the 100 bar CO_2 (pink), 100 bar H_2O (blue), and 100 bar CH_4 (green) atmospheric scenarios for L168-9 b, compared to the expected dayside emission temperature of a bare rock (1200 K assuming an albedo of 0.1; black vertical dashed line). The colored dashed curves are the $15 \mu\text{m}$ emission contribution function (Equation 4 from Lothringer et al. 2018) for each atmospheric scenario. *Right:* Simulated JWST/MIRI eclipse depths at $15 \mu\text{m}$ for three eclipse observations (points) based on each scenario. The bare rock case is represented by a 1200 K blackbody.

Gaussian noise (i.e., the synthetic data are centered on truth).

We find that the 100 bar CO_2 scenario has a relatively cold upper atmosphere because CO_2 emits efficiently in the infrared and is fairly transparent to the incident M-dwarf radiation. The result is a small ~ 60 ppm dayside emission signal at $15 \mu\text{m}$, which could be distinguished from a bare rock (127 ppm emission) at $\sim 4\sigma$ confidence for our assumed data quality. On the other hand, the H_2O and CH_4 cases absorb near-infrared starlight leading to warm upper atmospheres with large dayside emission fluxes that are more comparable to that of a bare rock (Lincowski et al. 2024). $15 \mu\text{m}$ emission from an H_2O -dominated atmosphere is 2.3σ smaller than the bare rock scenario, while a CH_4 atmosphere has a dayside flux within 1σ of the bare rock case. However, with the rapid loss of hydrogen to space discussed in Section 5.2, it is perhaps unlikely for atmospheres rich in H-bearing species (e.g., steam or CH_4) to persist over the 3 Gyr lifetime of this planet.

6. SUMMARY & CONCLUSIONS

We assembled the complete near- to mid-infrared transmission spectrum of the rocky planet L 168-9 b us-

ing three transit observations with NIRSpec/G395H, combined with mid-infrared MIRI/LRS commissioning data (Bouwman et al. 2023). Based on the 3–12 μm transmission spectrum of this target observed with JWST, our key results on this planet’s atmospheric properties are summarized below.

- The near- to mid-infrared transmission spectrum of L 168-9 b shows a lack of discernible atmospheric features (Figure 7). Fits to 1D thermochemical equilibrium forward models reveal that the data prefer single gas models and a flat line model over $25\text{--}100\times$ solar models, while near-solar models possess intermediate goodness of fit, likely due to the lack of high amplitude spectral features at the wavelengths of interest. These results suggest a high atmospheric mean molecular weight ($>4 \text{ g mol}^{-1}$), the presence of high altitude aerosols, or the lack of an atmosphere altogether (Figure 8).
- While L 168-9 b’s high bulk density (Figure 9) already makes low mean molecular weight atmospheres unlikely, we also ran atmospheric escape models for a range of initial atmospheric mass fractions (2–100%) to evaluate whether small amounts

of light gasses can remain on the planet. Based on these models, however, any significant primordial H₂/He atmosphere on L 168-9 b would be removed within 200 Myr (Figure 10).

- 15 μ m MIRI eclipse observations could provide a discerning lens to distinguish between the high mean molecular weight and no atmosphere scenarios for L 168-9 b. With three eclipse observations, we should be able to confidently identify a CO₂-dominated atmosphere if one exists, while emission from atmospheres of other compositions would be more challenging to distinguish from the bare rock scenario.

ACKNOWLEDGMENTS

This work is based on observations made with the NASA/ESA/CSA James Webb Space Telescope. The data were obtained from the Mikulski Archive for Space Telescopes at the Space Telescope Science Institute, which is operated by the Association of Universities for Research in Astronomy, Inc., under NASA contract NAS

5-03127 for JWST. The specific observations analyzed can be accessed via [10.17909/q5hp-7b93](https://doi.org/10.17909/q5hp-7b93). These observations are associated with program #2512. Support for program #2512 was provided by NASA through a grant from the Space Telescope Science Institute, which is operated by the Association of Universities for Research in Astronomy, Inc., under NASA contract NAS 5-03127. This work benefitted from the 2022 and 2023 Exoplanet Summer Program in the Other Worlds Laboratory (OWL) at the University of California, Santa Cruz, a program funded by the Heising-Simons Foundation. This work is funded in part by the Alfred P. Sloan Foundation under grant G202114194.

Co-author contributions are as follows: M.K.A. led the data analysis and write-up of this study. P.G. led the modeling efforts. J.I.A.R. and N.L.W. provided additional independent reductions. N.F.W. A.A., and A.D. aided in the theoretical interpretation of the data, respectively contributing climate models and simulated MIRI data, interior modeling, and photoevaporation models. All authors read and provided comments & conversations that greatly improved the quality of the manuscript.

REFERENCES

- Airapetian, V. S., Glocer, A., Khazanov, G. V., et al. 2017, *ApJL*, 836, L3, doi: [10.3847/2041-8213/836/1/L3](https://doi.org/10.3847/2041-8213/836/1/L3)
- Alderson, L., Wakeford, H. R., Alam, M. K., et al. 2023, *Nature*, 614, 664, doi: [10.1038/s41586-022-05591-3](https://doi.org/10.1038/s41586-022-05591-3)
- Alderson, L., Batalha, N. E., Wakeford, H. R., et al. 2024, *AJ*, 167, 216, doi: [10.3847/1538-3881/ad32c9](https://doi.org/10.3847/1538-3881/ad32c9)
- Asplund, M., Grevesse, N., Sauval, A. J., & Scott, P. 2009, *ARA&A*, 47, 481, doi: [10.1146/annurev.astro.46.060407.145222](https://doi.org/10.1146/annurev.astro.46.060407.145222)
- Astudillo-Defru, N., Cloutier, R., Wang, S. X., et al. 2020, *A&A*, 636, A58, doi: [10.1051/0004-6361/201937179](https://doi.org/10.1051/0004-6361/201937179)
- Batalha, N., Freedman, R., Lupu, R., & Marley, M. 2020, *Resampled Opacity Database for PICASO v2, 1.0*, Zenodo, doi: [10.5281/zenodo.3759675](https://doi.org/10.5281/zenodo.3759675)
- Batalha, N. E., Marley, M. S., Lewis, N. K., & Fortney, J. J. 2019, *ApJ*, 878, 70, doi: [10.3847/1538-4357/ab1b51](https://doi.org/10.3847/1538-4357/ab1b51)
- Batalha, N. E., Wolfgang, A., Teske, J., et al. 2023, *AJ*, 165, 14, doi: [10.3847/1538-3881/ac9f45](https://doi.org/10.3847/1538-3881/ac9f45)
- Bell, T., Ahrer, E.-M., Brande, J., et al. 2022, *The Journal of Open Source Software*, 7, 4503, doi: [10.21105/joss.04503](https://doi.org/10.21105/joss.04503)
- Bell, T. J., Kreidberg, L., Kendrew, S., et al. 2023, arXiv e-prints, arXiv:2301.06350, doi: [10.48550/arXiv.2301.06350](https://doi.org/10.48550/arXiv.2301.06350)
- Birkmann, S. M., Ferruit, P., Giardino, G., et al. 2022, *A&A*, 661, A83, doi: [10.1051/0004-6361/202142592](https://doi.org/10.1051/0004-6361/202142592)
- Borges, S. R., Jones, G. G., & Robinson, T. D. 2024, *Astrobiology*, 24, 283, doi: [10.1089/ast.2023.0099](https://doi.org/10.1089/ast.2023.0099)
- Bouwman, J., Kendrew, S., Greene, T. P., et al. 2023, *PASP*, 135, 038002, doi: [10.1088/1538-3873/acbc49](https://doi.org/10.1088/1538-3873/acbc49)
- Bushouse, H., Eisenhamer, J., Dencheva, N., et al. 2022, *JWST Calibration Pipeline, 1.8.5*, Zenodo, Zenodo, doi: [10.5281/zenodo.7429939](https://doi.org/10.5281/zenodo.7429939)
- Checlair, J. H., Villanueva, G. L., Hayworth, B. P. C., et al. 2021, *AJ*, 161, 150, doi: [10.3847/1538-3881/abdb36](https://doi.org/10.3847/1538-3881/abdb36)
- Claret, A. 2000, *A&A*, 363, 1081
- Currie, M. H., Meadows, V. S., & Rasmussen, K. C. 2023, *PSJ*, 4, 83, doi: [10.3847/PSJ/accf86](https://doi.org/10.3847/PSJ/accf86)
- Damiano, M., Bello-Arufe, A., Yang, J., & Hu, R. 2024, arXiv e-prints, arXiv:2403.13265, doi: [10.48550/arXiv.2403.13265](https://doi.org/10.48550/arXiv.2403.13265)
- Damiano, M., Hu, R., Barclay, T., et al. 2022, *AJ*, 164, 225, doi: [10.3847/1538-3881/ac9472](https://doi.org/10.3847/1538-3881/ac9472)
- de Wit, J., Wakeford, H. R., Gillon, M., et al. 2016, *Nature*, 537, 69, doi: [10.1038/nature18641](https://doi.org/10.1038/nature18641)
- de Wit, J., Wakeford, H. R., Lewis, N. K., et al. 2018, *Nature Astronomy*, 2, 214, doi: [10.1038/s41550-017-0374-z](https://doi.org/10.1038/s41550-017-0374-z)

- Defrère, D., Léger, A., Absil, O., et al. 2018, *Experimental Astronomy*, 46, 543, doi: [10.1007/s10686-018-9613-2](https://doi.org/10.1007/s10686-018-9613-2)
- Diamond-Lowe, H., Berta-Thompson, Z., Charbonneau, D., & Kempton, E. M. R. 2018, *AJ*, 156, 42, doi: [10.3847/1538-3881/aac6dd](https://doi.org/10.3847/1538-3881/aac6dd)
- Diamond-Lowe, H., Charbonneau, D., Malik, M., Kempton, E. M. R., & Beletsky, Y. 2020, *AJ*, 160, 188, doi: [10.3847/1538-3881/abaf4f](https://doi.org/10.3847/1538-3881/abaf4f)
- Diamond-Lowe, H., Mendonça, J. M., Charbonneau, D., & Buchhave, L. A. 2023, *AJ*, 165, 169, doi: [10.3847/1538-3881/acbf39](https://doi.org/10.3847/1538-3881/acbf39)
- Dong, C., Jin, M., Lingam, M., et al. 2018, *Proceedings of the National Academy of Science*, 115, 260, doi: [10.1073/pnas.1708010115](https://doi.org/10.1073/pnas.1708010115)
- Dos Santos, L. A., Alam, M. K., Espinoza, N., & Vissapragada, S. 2023, *AJ*, 165, 244, doi: [10.3847/1538-3881/accf10](https://doi.org/10.3847/1538-3881/accf10)
- Dressing, C. D., & Charbonneau, D. 2015, *ApJ*, 807, 45, doi: [10.1088/0004-637X/807/1/45](https://doi.org/10.1088/0004-637X/807/1/45)
- Engle, S. G., & Guinan, E. F. 2023, *ApJL*, 954, L50, doi: [10.3847/2041-8213/acf472](https://doi.org/10.3847/2041-8213/acf472)
- Foreman-Mackey, D., Hogg, D. W., Lang, D., & Goodman, J. 2013, *PASP*, 125, 306, doi: [10.1086/670067](https://doi.org/10.1086/670067)
- Gordon, S., & McBride, B. J. 1994, *Computer program for calculation of complex chemical equilibrium compositions and applications. Part 1: Analysis*, Tech. rep.
- Grant, D., Valentine, D., & Wakeford, H. R. 2023, *Exo-TiC/ExoTiC-MIRI: ExoTiC-MIRI v1.0.0, v1.0.0*, Zenodo, Zenodo, doi: [10.5281/zenodo.8211207](https://doi.org/10.5281/zenodo.8211207)
- Grant, D., & Wakeford, H. R. 2022, *Exo-TiC/ExoTiC-LD: ExoTiC-LD v3.0.0, v3.0.0*, Zenodo, doi: [10.5281/zenodo.7437681](https://doi.org/10.5281/zenodo.7437681)
- Greene, T. P., Bell, T. J., Ducrot, E., et al. 2023, *Nature*, 618, 39, doi: [10.1038/s41586-023-05951-7](https://doi.org/10.1038/s41586-023-05951-7)
- Greene, T. P., Line, M. R., Montero, C., et al. 2016, *ApJ*, 817, 17, doi: [10.3847/0004-637X/817/1/17](https://doi.org/10.3847/0004-637X/817/1/17)
- Guillot, T. 2010, *A&A*, 520, A27, doi: [10.1051/0004-6361/200913396](https://doi.org/10.1051/0004-6361/200913396)
- Hall, S., Krissansen-Totton, J., Robinson, T., Salvador, A., & Fortney, J. J. 2023, *AJ*, 166, 254, doi: [10.3847/1538-3881/ad03e9](https://doi.org/10.3847/1538-3881/ad03e9)
- Hawker, G. A., & Parry, I. R. 2019, *MNRAS*, 484, 4855, doi: [10.1093/mnras/stz323](https://doi.org/10.1093/mnras/stz323)
- Hu, R., Bello-Arufe, A., Zhang, M., et al. 2024, *arXiv e-prints*, arXiv:2405.04744, doi: [10.48550/arXiv.2405.04744](https://doi.org/10.48550/arXiv.2405.04744)
- Jakobsen, P., Ferruit, P., Alves de Oliveira, C., et al. 2022, *A&A*, 661, A80, doi: [10.1051/0004-6361/202142663](https://doi.org/10.1051/0004-6361/202142663)
- Kane, S. R., Roettenbacher, R. M., Unterborn, C. T., Foley, B. J., & Hill, M. L. 2020, *PSJ*, 1, 36, doi: [10.3847/PSJ/abaab5](https://doi.org/10.3847/PSJ/abaab5)
- Kasting, J. F., & Pollack, J. B. 1983, *Icarus*, 53, 479, doi: [10.1016/0019-1035\(83\)90212-9](https://doi.org/10.1016/0019-1035(83)90212-9)
- Kendrew, S., Scheithauer, S., Bouchet, P., et al. 2015, *PASP*, 127, 623, doi: [10.1086/682255](https://doi.org/10.1086/682255)
- Kendrew, S., Dicken, D., Bouwman, J., et al. 2018, in *Society of Photo-Optical Instrumentation Engineers (SPIE) Conference Series*, Vol. 10698, *Space Telescopes and Instrumentation 2018: Optical, Infrared, and Millimeter Wave*, ed. M. Lystrup, H. A. MacEwen, G. G. Fazio, N. Batalha, N. Siegler, & E. C. Tong, 106983U, doi: [10.1117/12.2313951](https://doi.org/10.1117/12.2313951)
- Kirk, J., López-Morales, M., Wheatley, P. J., et al. 2019, *AJ*, 158, 144, doi: [10.3847/1538-3881/ab397d](https://doi.org/10.3847/1538-3881/ab397d)
- Kirk, J., Wheatley, P. J., Louden, T., et al. 2018, *MNRAS*, 474, 876, doi: [10.1093/mnras/stx2826](https://doi.org/10.1093/mnras/stx2826)
- Kirk, J., Rackham, B. V., MacDonald, R. J., et al. 2021, *AJ*, 162, 34, doi: [10.3847/1538-3881/abfcd2](https://doi.org/10.3847/1538-3881/abfcd2)
- Kirk, J., Stevenson, K. B., Fu, G., et al. 2024, *AJ*, 167, 90, doi: [10.3847/1538-3881/ad19df](https://doi.org/10.3847/1538-3881/ad19df)
- Kite, E. S., & Barnett, M. N. 2020, *Proceedings of the National Academy of Science*, 117, 18264, doi: [10.1073/pnas.2006177117](https://doi.org/10.1073/pnas.2006177117)
- Koll, D. D. B. 2022, *ApJ*, 924, 134, doi: [10.3847/1538-4357/ac3b48](https://doi.org/10.3847/1538-4357/ac3b48)
- Kostogryz, N., Shapiro, A., Witzke, V., et al. 2023, *Research Notes of the AAS*, 7, 39
- Kostogryz, N., Witzke, V., Shapiro, A., et al. 2022, *Astronomy & Astrophysics*, 666, A60
- Kreidberg, L. 2015, *PASP*, 127, 1161, doi: [10.1086/683602](https://doi.org/10.1086/683602)
- Kreidberg, L., Koll, D. D. B., Morley, C., et al. 2019, *Nature*, 573, 87, doi: [10.1038/s41586-019-1497-4](https://doi.org/10.1038/s41586-019-1497-4)
- Krissansen-Totton, J. 2023, *ApJL*, 951, L39, doi: [10.3847/2041-8213/acdc26](https://doi.org/10.3847/2041-8213/acdc26)
- Krissansen-Totton, J., & Fortney, J. J. 2022, *ApJ*, 933, 115, doi: [10.3847/1538-4357/ac69cb](https://doi.org/10.3847/1538-4357/ac69cb)
- Leung, M., Meadows, V. S., & Lustig-Yaeger, J. 2020, *AJ*, 160, 11, doi: [10.3847/1538-3881/ab9012](https://doi.org/10.3847/1538-3881/ab9012)
- Lichtenberg, T., & Clement, M. S. 2022, *ApJL*, 938, L3, doi: [10.3847/2041-8213/ac9521](https://doi.org/10.3847/2041-8213/ac9521)
- Lim, O., Benneke, B., Doyon, R., et al. 2023, *ApJL*, 955, L22, doi: [10.3847/2041-8213/acf7c4](https://doi.org/10.3847/2041-8213/acf7c4)
- Lincowski, A., Virtual Planetary Laboratory, Meadows, V., et al. 2024, in *AAS/Division for Extreme Solar Systems Abstracts*, Vol. 56, *AAS/Division for Extreme Solar Systems Abstracts*, 627.10
- Line, M. R., Wolf, A. S., Zhang, X., et al. 2013, *ApJ*, 775, 137, doi: [10.1088/0004-637X/775/2/137](https://doi.org/10.1088/0004-637X/775/2/137)

- Lothringer, J. D., Barman, T., & Koskinen, T. 2018, *ApJ*, 866, 27, doi: [10.3847/1538-4357/aadd9e](https://doi.org/10.3847/1538-4357/aadd9e)
- Luger, R., & Barnes, R. 2015, *Astrobiology*, 15, 119, doi: [10.1089/ast.2014.1231](https://doi.org/10.1089/ast.2014.1231)
- Lustig-Yaeger, J., Fu, G., May, E. M., et al. 2023, *Nature Astronomy*, 7, 1317, doi: [10.1038/s41550-023-02064-z](https://doi.org/10.1038/s41550-023-02064-z)
- Mansfield, M., Kite, E. S., Hu, R., et al. 2019, *ApJ*, 886, 141, doi: [10.3847/1538-4357/ab4c90](https://doi.org/10.3847/1538-4357/ab4c90)
- Marcus, R. A., Sasselov, D., Hernquist, L., & Stewart, S. T. 2010, *ApJL*, 712, L73, doi: [10.1088/2041-8205/712/1/L73](https://doi.org/10.1088/2041-8205/712/1/L73)
- Matsuo, T., Dannert, F., Laugier, R., et al. 2023, *A&A*, 678, A97, doi: [10.1051/0004-6361/202345927](https://doi.org/10.1051/0004-6361/202345927)
- May, E. M., MacDonald, R. J., Bennett, K. A., et al. 2023, *ApJL*, 959, L9, doi: [10.3847/2041-8213/ad054f](https://doi.org/10.3847/2041-8213/ad054f)
- Moran, S. E., Hörst, S. M., Batalha, N. E., Lewis, N. K., & Wakeford, H. R. 2018, *AJ*, 156, 252, doi: [10.3847/1538-3881/aae83a](https://doi.org/10.3847/1538-3881/aae83a)
- Moran, S. E., Stevenson, K. B., Sing, D. K., et al. 2023, *ApJL*, 948, L11, doi: [10.3847/2041-8213/accb9c](https://doi.org/10.3847/2041-8213/accb9c)
- Mukherjee, S., Batalha, N. E., Fortney, J. J., & Marley, M. S. 2023, *The Astrophysical Journal*, 942, 71, doi: [10.3847/1538-4357/ac9f48](https://doi.org/10.3847/1538-4357/ac9f48)
- Owen, J. E., & Jackson, A. P. 2012, *MNRAS*, 425, 2931, doi: [10.1111/j.1365-2966.2012.21481.x](https://doi.org/10.1111/j.1365-2966.2012.21481.x)
- Owen, J. E., & Wu, Y. 2017, *ApJ*, 847, 29, doi: [10.3847/1538-4357/aa890a](https://doi.org/10.3847/1538-4357/aa890a)
- Pineda, J. S., Youngblood, A., & France, K. 2021, *ApJ*, 911, 111, doi: [10.3847/1538-4357/abe8d7](https://doi.org/10.3847/1538-4357/abe8d7)
- Pont, F., Zucker, S., & Queloz, D. 2006, *MNRAS*, 373, 231, doi: [10.1111/j.1365-2966.2006.11012.x](https://doi.org/10.1111/j.1365-2966.2006.11012.x)
- Pontoppidan, K. M., Pickering, T. E., Laidler, V. G., et al. 2016, in *Society of Photo-Optical Instrumentation Engineers (SPIE) Conference Series*, Vol. 9910, *Observatory Operations: Strategies, Processes, and Systems VI*, ed. A. B. Peck, R. L. Seaman, & C. R. Benn, 991016, doi: [10.1117/12.2231768](https://doi.org/10.1117/12.2231768)
- Quanz, S. 2021, in *43rd COSPAR Scientific Assembly*. Held 28 January - 4 February, Vol. 43, 507
- Quanz, S. P., Absil, O., Benz, W., et al. 2022, *Experimental Astronomy*, 54, 1197, doi: [10.1007/s10686-021-09791-z](https://doi.org/10.1007/s10686-021-09791-z)
- Redfield, S., Batalha, N., Benneke, B., et al. 2024, *arXiv e-prints*, arXiv:2404.02932, doi: [10.48550/arXiv.2404.02932](https://doi.org/10.48550/arXiv.2404.02932)
- Ressler, M. E., Sukhatme, K. G., Franklin, B. R., et al. 2015, *PASP*, 127, 675, doi: [10.1086/682258](https://doi.org/10.1086/682258)
- Rieke, G. H., Wright, G. S., Böker, T., et al. 2015a, *PASP*, 127, 584, doi: [10.1086/682252](https://doi.org/10.1086/682252)
- Rieke, G. H., Ressler, M. E., Morrison, J. E., et al. 2015b, *PASP*, 127, 665, doi: [10.1086/682257](https://doi.org/10.1086/682257)
- Rogers, J. G., & Owen, J. E. 2021, *MNRAS*, 503, 1526, doi: [10.1093/mnras/stab529](https://doi.org/10.1093/mnras/stab529)
- Rogers, L. A. 2015, *ApJ*, 801, 41, doi: [10.1088/0004-637X/801/1/41](https://doi.org/10.1088/0004-637X/801/1/41)
- Rustamkulov, Z., Sing, D. K., Liu, R., & Wang, A. 2022, *ApJL*, 928, L7, doi: [10.3847/2041-8213/ac5b6f](https://doi.org/10.3847/2041-8213/ac5b6f)
- Scarsdale et al. 2024, submitted, *The Astronomical Journal*
- Schaefer, L., Wordsworth, R. D., Berta-Thompson, Z., & Sasselov, D. 2016, *ApJ*, 829, 63, doi: [10.3847/0004-637X/829/2/63](https://doi.org/10.3847/0004-637X/829/2/63)
- Seager, S., & Sasselov, D. D. 2000, *ApJ*, 537, 916, doi: [10.1086/309088](https://doi.org/10.1086/309088)
- Shkolnik, E. L., & Barman, T. S. 2014, *AJ*, 148, 64, doi: [10.1088/0004-6256/148/4/64](https://doi.org/10.1088/0004-6256/148/4/64)
- Snellen, I., de Kok, R., Birkby, J. L., et al. 2015, *A&A*, 576, A59, doi: [10.1051/0004-6361/201425018](https://doi.org/10.1051/0004-6361/201425018)
- Stevenson, K. B. 2016, *ApJL*, 817, L16, doi: [10.3847/2041-8205/817/2/L16](https://doi.org/10.3847/2041-8205/817/2/L16)
- Vaughan, S. R., Gebhard, T. D., Bott, K., et al. 2023, *MNRAS*, 524, 5477, doi: [10.1093/mnras/stad2127](https://doi.org/10.1093/mnras/stad2127)
- Wakeford, H. R., Lewis, N. K., Fowler, J., et al. 2019, *AJ*, 157, 11, doi: [10.3847/1538-3881/aaf04d](https://doi.org/10.3847/1538-3881/aaf04d)
- Wallack, N. L., Batalha, N. E., Alderson, L., et al. 2024, *arXiv e-prints*, arXiv:2404.01264, doi: [10.48550/arXiv.2404.01264](https://doi.org/10.48550/arXiv.2404.01264)
- Wogan, N. 2023, *PhotochemPy: 1-D photochemical model of rocky planet atmospheres*, *Astrophysics Source Code Library*, record ascl:2312.011
- Wright, G. S., Rieke, G. H., Glasse, A., et al. 2023, *PASP*, 135, 048003, doi: [10.1088/1538-3873/acbe66](https://doi.org/10.1088/1538-3873/acbe66)
- Wright, N. J., Drake, J. J., Mamajek, E. E., & Henry, G. W. 2011, *ApJ*, 743, 48, doi: [10.1088/0004-637X/743/1/48](https://doi.org/10.1088/0004-637X/743/1/48)
- Zeng, L., Sasselov, D. D., & Jacobsen, S. B. 2016, *ApJ*, 819, 127, doi: [10.3847/0004-637X/819/2/127](https://doi.org/10.3847/0004-637X/819/2/127)
- Zhang, H., Wang, J., & Plummer, M. K. 2024a, *AJ*, 167, 37, doi: [10.3847/1538-3881/ad109e](https://doi.org/10.3847/1538-3881/ad109e)
- Zhang, M., Hu, R., Inglis, J., et al. 2024b, *ApJL*, 961, L44, doi: [10.3847/2041-8213/ad1a07](https://doi.org/10.3847/2041-8213/ad1a07)
- Zieba, S., Kreidberg, L., Ducrot, E., et al. 2023, *Nature*, 620, 746, doi: [10.1038/s41586-023-06232-z](https://doi.org/10.1038/s41586-023-06232-z)